JACS
JOURNAL OF THE AMERICAN CHEMICAL SOCIETY

ARTICLE

pubs.acs.org/JACS

Photodynamics and Time-Resolved Fluorescence of Azobenzene in Solution: A Mixed Quantum-Classical Simulation

Teresa Cusati, Giovanni Granucci, and Maurizio Persico*

Dipartimento di Chimica e Chimica Industriale, Università di Pisa, v. Risorgimento 35, I-56126 Pisa, Italy

Supporting Information

ABSTRACT: We have simulated the photodynamics of azobenzene by means of the Surface Hopping method. We have considered both the *trans* → *cis* and the *cis* → *trans* processes, caused by excitation in the $n \rightarrow \pi^*$ band (S_1 state). To bring out the solvent effects on the excited state dynamics, we have run simulations in four different environments: in vacuo, in *n*-hexane, in methanol, and in ethylene glycol. Our simulations reproduce very well the measured quantum yields and the time dependence of the intensity and anisotropy of the transient fluorescence. Both the photoisomerization and the $S_1 \rightarrow S_0$ internal conversion require the torsion of the N═N double bond, but the N—C bond rotations and the NNC bending vibrations also play a role. In the *trans* → *cis* photoconversion the N═N torsional motion and the excited state decay are delayed by increasing the solvent viscosity, while the *cis* → *trans* processes are less affected. The analysis of the simulation results allows the experimental observations to be explained in detail, and in particular the counterintuitive increase of the *trans* → *cis* quantum yield with viscosity, as well as the relationship between the excited state dynamics and the solvent effects on the fluorescence lifetimes and depolarization.

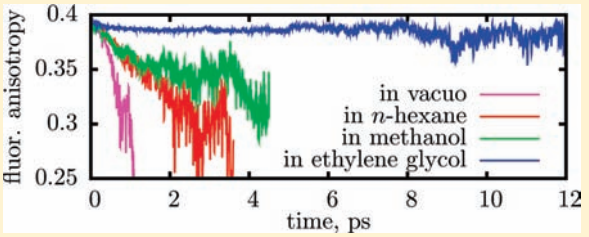

1. INTRODUCTION AND STATE OF THE ART

This paper presents a computational simulation of the $n \rightarrow \pi^*$ photodynamics of *trans*- and *cis*-azobenzene (TAB and CAB, respectively), in vacuo and in three different solvents. The photoisomerization and the decay of the excited states of azobenzene have been the object of many experimental[1−27] and theoretical[28−47] investigations, because of the basic questions about the mechanism and because azobenzene has been used as the photoactive unit in a wide variety of nanoscale devices and compounds with photomodulable properties (see reviews[48−54] and some recent applications[55−68]). The proposed applications use light of the appropriate wavelength and polarization to power molecular machines,[48,50,54,60,67] control electrical switches,[59] displace chemical equilibria,[48,51] trigger enzymatic activity and peptide folding,[51,53] and change the properties of photoresponsive materials of interest in optics,[52,53,55,56,58,68] electronics,[49] mechanical actuators,[53,61,64−66] data storage,[63] and other fields. In most of these examples, the (super)molecular structures surrounding the azobenzene chromophore are modified because of its isomerization. The fact that azobenzene is able to isomerize in a variety of environments, some of which are very constraining,[42,43] is therefore crucial in such applications. Viscous solvents are typical media that may hinder large amplitude geometry changes occurring in photochemical reactions, and some interesting experimental studies[2,25] have investigated the effect of viscosity on the photodynamics of azobenzene, as we do theoretically in the present work.

The fundamental mechanistic questions concern the photoreaction pathway and the competition between excited state decay and isomerization, which determines the quantum yields. In low viscosity solvents, by irradiation in the $n \rightarrow \pi^*$ band (S_1 state), the *trans* → *cis* photoisomerization quantum yields $\Phi_{t\rightarrow c}$ range from 0.20 to 0.36.[38] In the same conditions, by excitation to the $\pi \rightarrow \pi^*$ states (S_2-S_4) the $\Phi_{t\rightarrow c}$ yield is smaller by about a factor of 2. A similar dependence on the wavelength is observed for the reverse *cis* → *trans* photoconversion, but in general $\Phi_{c\rightarrow t}$ is larger than $\Phi_{t\rightarrow c}$: with low viscosity and $n \rightarrow \pi^*$ irradiation, $\Phi_{c\rightarrow t}$ is in the range 0.40−0.69. The dependence of the quantum yields on the absorption band led to the postulation of two different mechanisms for the photoisomerization:[7−10] torsion of the N═N double bond for the $n \rightarrow \pi^*$ excitation and N-inversion for the $\pi \rightarrow \pi^*$ one. This interpretation was supported by the first computational attempt to characterize the excited potential energy surfaces (PES) of azobenzene, by Monti et al. in 1982.[28] Only in 1999 an ab initio study based on CASSCF and second order perturbation CI showed that the torsional mechanism is energetically preferable both in the S_1 and in the S_2 states, although the N-inversion might also be viable, at least for the $n \rightarrow \pi^*$ *cis* → *trans* conversion.[29] These findings have since then been confirmed by more accurate and/or more extensive explorations of the PES.[30−33,37,44,45] In particular, Ishikawa et al.[30] produced maps of the S_0, S_1, and S_2 PES, as functions of the torsional and inversional reaction coordinates, by CASSCF calculations. They also identified the S_0-S_1 conical intersection (CI) close to the minimum of S_1, that is, at a CNNC torsional angle of about 90°. Diau[31] found that the S_0 and S_1 surfaces also cross at a transoid (planar) geometry, along the symmetric NNC bending

Received: December 30, 2010
Published: March 14, 2011

dx.doi.org/10.1021/ja1113529 | J. Am. Chem. Soc. 2011, 133, 5109–5123

coordinate, that is, by opening both NNC angles. Orlandi and his group[33,44] determined the CIs with higher lying states and showed that the S_0-S_1 CIs found by torsion and by symmetric inversion belong to the same crossing seam. Their CASSCF and CASPT2 calculations are probably the most accurate ones performed on azobenzene to date.

The mere inspection of the PES cannot provide more than a hypothetical rationalization of the wavelength dependence of the quantum yields. To put the interpretation of such observations on firmer ground and describe the reaction mechanism, our group performed a full set of single molecule simulations, for the *trans* → *cis* and *cis* → *trans* photoconversions with $n \rightarrow \pi^*$ and with $\pi \rightarrow \pi^*$ excitation.[34,38] We used the Surface Hopping (SH) approach,[69] with PES and couplings computed on the fly by a semiempirical method with an ad hoc reparameterization.[70] The simulation results were in rather good agreement with the experimental quantum yields. We showed that, after $\pi \rightarrow \pi^*$ excitation, the S_2 state decays very fast (≈0.1 ps) to S_1. Once on the S_1 surface, either by direct $n \rightarrow \pi^*$ excitation or by internal conversion (IC) from S_2, the dynamics follows essentially the torsional mechanism, at least until the midpoint (CNNC ≈ 90°) is reached. Near such a twisted geometry the minimum energy path in S_1 meets the S_0-S_1 crossing seam, and the conversion to the ground state is very likely. By $\pi \rightarrow \pi^*$ excitation and subsequent decay to S_1, the vibrational energy excess is larger than in the case of direct $n \rightarrow \pi^*$ excitation; in particular, the symmetric NNC bending mode of TAB gets more excited. As a consequence, the IC to the ground state takes place earlier, that is, closer to the starting isomer geometry: this is why the $\pi \rightarrow \pi^*$ quantum yields are lower than the $n \rightarrow \pi^*$ ones. Our simulations therefore explain the wavelength dependence of the quantum yields as due to shifting the balance between the competing processes of isomerization and internal conversion, within one basic mechanism (torsion of the N═N double bond).

A wealth of data about the excited state dynamics were obtained in the last 15 years through transient spectroscopy techniques. Here we shall focus on the n → π^* photodynamics, which is the object of this paper. Time-resolved differential absorption[12,13,15,23,24] and up-converted fluorescence[21,25] measurements in low viscosity solvents show a biexponential decay of the S_1 state: the more important component has lifetimes of 0.15−0.6 ps, and the longer tail is in the range 0.6−3 ps. The CAB photodynamics is also biexponential but faster, with short lifetimes of 0.10−0.18 ps and long ones of 0.9−2 ps, obtained by transient absorption.[13,23] Recent resonant Raman measurements by the Mathies group[27] showed that the short time dynamics in the S_1 state of TAB is dominated by the NNC bending mode and that of CAB by the CNNC torsion (in both cases also the NN and CN stretching modes play a role). On the basis of our simulations[34,38] we had predicted the possibility of observing the NNC bending vibration in TAB by resonant Raman spectroscopy, because this mode is excited in S_1, where the equilibrium angle is much larger than in S_0; and also, we had found a much faster CNNC torsion in CAB, such as to override the NNC bending motion. As to the S_1 state lifetimes, our results were consistent with the fast component of both the *trans*- and the *cis*-azobenzene decays, but did not match the slow one. This partial discrepancy could be due to one or more approximations inherent to our model: for instance, the slope of the S_1 PES could have been slightly overestimated, so as to accelerate the torsional motion; or, the surface hopping algorithm might not reproduce adequately the real quantum wavepacket dynamics. In a previous work,[36] we compared the Surface Hopping results with those of Full Multiple Spawning (FMS)[71] wavepacket dynamics. While the basic features of the mechanism and of the nonadiabatic dynamics were confirmed, some quantitative differences between the two treatments were apparent. In particular, the SH treatment in certain conditions overestimates the decay rates from upper to lower electronic states. In a later paper[72] we have introduced in the SH algorithm a quantum decoherence correction that improves the agreement with quantum wavepacket calculations and will be used in the present work.

Probably the most important source of variance between our previous simulations[34,38] and the transient spectroscopy measurements is that almost all the experiments were run in the condensed phase, while we computed the single molecule dynamics. In fact, in the one case where lifetimes were measured in a jet of azobenzene molecules,[22] they were all found shorter than 0.5 ps ($\pi \rightarrow \pi^*$ excitation, with time-resolved photoelectron spectroscopy as the probe technique). As we shall see more in detail in the next sections, the quantum yields and the lifetimes are strongly affected by the solvent viscosity. Chang et al.[25] obtained an especially intriguing set of results by measuring the decay of fluorescence intensity and anisotropy of TAB in *n*-hexane and ethylene glycol: the latter solvent not only slows down the decay of the S_1 state but also suppresses almost completely the fluorescence depolarization. Solvent effects are therefore quite important, and one cannot exclude that they would alter substantially the reaction mechanism. Recent molecular dynamics simulations of the *trans* → *cis* photoisomerization by Tiberio et al.,[47] run with an empirical scheme for nonadiabatic transitions, suggest that a mixed torsion−inversion mechanism is especially important in the condensed phase. However, in these simulations the reaction pathway only acquires a considerable N-inversional component after the molecule has reverted to the ground state, as already found in our work on the isolated molecule.[38] On the other hand, the crucial events that determine the quantum yield take place in the S_1 state (namely, the competition between progress along the reaction coordinate and nonadiabatic decay). Moreover, the force field employed by Tiberio et al.[47] only allows for the opening of one NNC bond angle, while we have shown that the NNC bending motion is symmetric[34] (see also Section 3 in this paper).

To clarify these matters we have run a set of simulations, of both the *trans* → *cis* and the *cis* → *trans* photoisomerizations, in three solvents with different polarity and viscosity properties: *n*-hexane, methanol, and ethylene glycol. Details of the method and of the PESs are given in the next section. In Section 3 we analyze the simulation results, and in Section 4 we present the computed fluorescence transients, with spectral and anisotropy data to be compared with the experimental ones.

2. METHOD AND POTENTIAL ENERGY SURFACES

2.1. Semiempirical Potential Energy Surfaces. We ran trajectory Surface Hopping simulations of the *trans* → *cis* and the *cis* → *trans* photodynamics, for the isolated azobenzene molecule (as a reference to evaluate the solvent effects) and with three solvents: *n*-hexane, methanol, and ethylene glycol (HEX, MeOH, and EG, respectively). The electronic energies and wave functions were computed on the fly by a semiempirical Configuration Interaction method based on SCF orbitals with floating occupation numbers (FOMO−CI), suited to represent reactive processes and excited states.[70] The configuration space was a

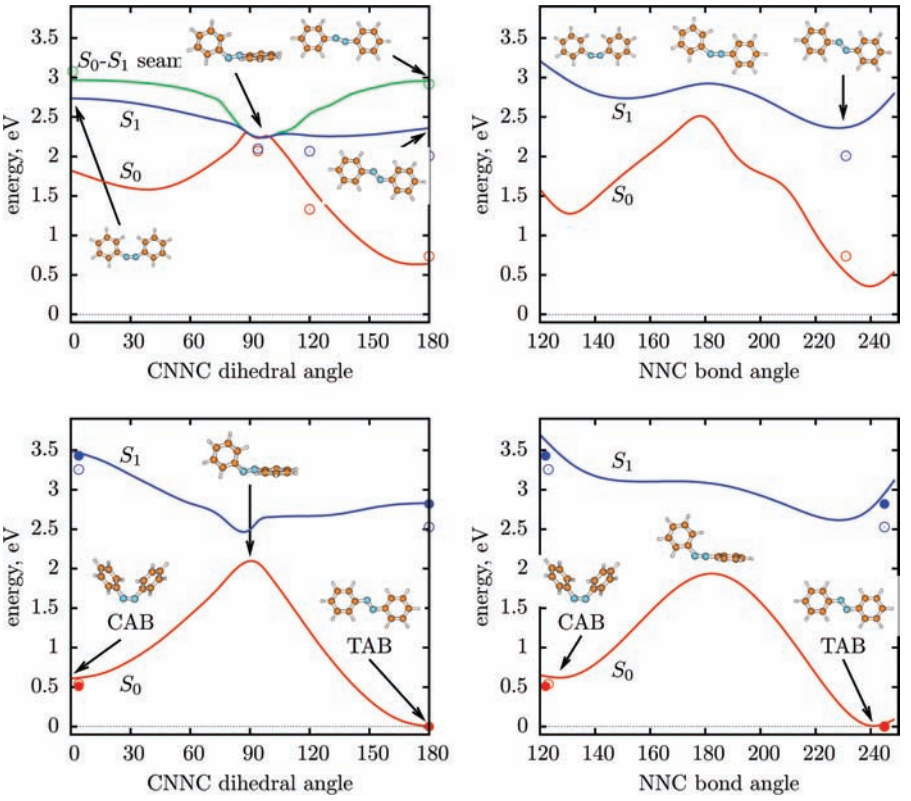

Figure 1. Potential energy curves of the S_0 and S_1 states, as functions of the torsional and of the inversional coordinates (CNNC dihedral and one of the NNC angles, respectively). All other internal coordinates are optimized, including the second NNC angle in the case of inversion. Ground state TAB is taken as the zero of the energy scale. Lower panels: geometries optimized for the S_0 state. Upper panels: geometries optimized for the S_1 state. The green curve in the upper left panel is the S_0-S_1 crossing seam. The open circles represent the ab initio CASPT2 results from Conti et al.[44] and the full circles the available experimental data. Some of the obtained structures are shown.

CAS with six electrons in four orbitals (two lone pairs of the N atoms, a π and a π^* MOs), plus all single excitations from seven occupied to six virtual orbitals (in total 94 Slater determinants). All the calculations were run by means of a development version of the MOPAC program,[73] with extensive additions introduced by our group.

The semiempirical parameters were optimized to yield accurate PES. Our previous parametrization[34] was revised, to take into account new ab initio results,[32,33] and to improve the torsional potential of the C—N bonds (details are given in a forthcoming paper[74]). In fact, a preliminary investigation of the $n \rightarrow \pi^*$ transition of TAB showed that the rotation of the phenyl groups around the C—N bonds is quite important in determining the transition dipole, which vanishes at the C_{2h} equilibrium geometry.[41] The reparameterization strategy was similar in the two cases.[34,74] From the available experimental and ab initio data we selected a set of target values $V_i^{(t)}$, mainly energies and geometrical parameters pertaining to extrema of the PESs. Next, we defined a function $S(\mathbf{P})$ of the semiempirical parameters $\mathbf{P}$, as a sum of weighted squared differences between the semiempirically computed values $V_i^{(s)}(P)$ and the targets $V_i^{(t)}$. The function $S(\mathbf{P})$ was then minimized by varying the parameters, using the simplex method combined with a form of simulated annealing. Only the N atom parameters were optimized, while for C we kept those previously determined for the benzene molecule and for H the standard AM1, as in our previous work.[34] We also added a potential term to improve the dependence of the PES on the NNC bond angles and on the NNCC dihedrals. All the details required to reproduce our electronic structure calculations are given in the Supporting Information.

The accuracy of the semiempirical PES is quite satisfactory, thanks to the reparameterization. The computed vertical excitation energies of TAB and CAB are 2.83 and 2.89 eV, while the absorption maxima in the vapor phase[75] yield 2.82 and 2.92 eV, respectively. By comparison, the latest CASPT2 calculations[44] yield 2.53 and 2.72 eV. Figure 1 shows the S_0 and S_1 potential energy curves for the torsional and the inversional pathways, along with the S_0-S_1 crossing seam. The results of Conti et al.[44] are shown for comparison by open circles, while the scanty experimental data are represented by full circles (they include the *cis*−*trans* energy difference[76] and the vertical excitation energies from spectral band maxima[75]). The semiempirical curves parallel the ab initio ones, with a small upward shift (increasing from CAB to TAB) due to the underestimation of the vertical transition energies by the CASPT2 calculations. Notice that the data by Conti et al.[44] were not yet available when the reparameterization was performed.

The crossing seam coincides with the minimum energy path (MEP) in S_1 along the torsional coordinate, for values of the CNNC dihedral angle between 90° and 100°. The global minimum of the S_1 PES and of the crossing seam is found at CNNC = 95°, 2.24 eV above the ground state TAB. The slope of the S_1 PES along the torsional pathway plays a key role in the dynamics: the Franck−Condon energies of TAB and CAB lie 0.59 and 1.27 eV above the minimum of S_1, while according to CASPT2 calculations[33,44] these values are 0.44 and 1.16 eV,

dx.doi.org/10.1021/ja1113529 |*J. Am. Chem. Soc.* 2011, 133, 5109–5123

respectively. The geometry optimization of TAB S_1 with planarity constraints yields a stabilization of 0.47 eV with respect to the Franck−Condon point (0.52 eV according to CASPT2), with the NNC angles opened to 132.3°. Outside the 90°−100° range of torsional angles the crossing seam is higher in energy than the S_1 MEP. The geometry deformation needed to reach the seam, starting from the MEP, is mainly the symmetric opening of both NNC angles. The inversional pathway in S_1 features a low barrier at NNC ≃ 180°, that lies below both the TAB and the CAB Franck−Condon points. The phenyl group adjacent to the inverting N atom prefers a perpendicular conformation (90° rotation around the C—N bond) in the S_0 transition state (TS), while in S_1 it remains in the molecular plane.

2.2. QM/MM Approach. The solvents have been represented by the all atom OPLS force-field.[77] In the case of EG we have adopted the ad hoc modifications of OPLS, proposed by Kony et al.[78] and by de Oliveira et al.[79] to study the thermodynamic properties of pure EG. The molecular mechanics (MM) description of the solvent and the quantum mechanical (QM) description of azobenzene (at semiempirical level) are combined in a hybrid QM/MM scheme with electrostatic embedding.[80] The QM/MM calculations have been run by linking MOPAC with the MM package TINKER.[81] The QM/MM interactions are in the form of a Lennard-Jones potential between the MM and the QM atoms, plus electrostatic interactions that are added to the semiempirical Hamiltonian. The electrostatic potential to which the QM nuclei and electrons are subjected is generated by the MM atomic charges. The latter had the standard OPLS values for HEX but were rescaled by the factor 0.41 for MeOH and EG (the scaling was not applied to the interactions between MM atoms). The scaling factor and the Lennard-Jones parameters have been determined to reproduce the results of MP2 calculations on the dimers of azobenzene with methane and methanol, chosen as representatives of alkanes and alcohols.[74] The methane−azobenzene interactions are very weak, with binding energies D_e = 0.042 and 0.049 eV for TAB and CAB, respectively, at the semiempirical QM/MM level. Methanol is hydrogen bound to both isomers, with D_e = 0.153 and 0.221 eV, which is less than the methanol−methanol interaction (0.262 eV, according to OPLS).

2.3. Initial Conditions. Each simulation consisted of about 600 trajectories, with initial conditions selected according to a Boltzmann distribution in the ground electronic state, weighted with the $S_0 \rightarrow S_1$ transition probability. We limited the initial excitation to the $n \rightarrow \pi^*$ band, by imposing a maximum of 3.4 eV to the transition energy, that is, the S_1-S_0 energy difference ΔE_{exc} at the initial geometry. The Boltzmann distribution of nuclear coordinates and momenta was obtained by running a Brownian trajectory.[82] The sampling takes into account the geometry dependent excitation probability, as described in a previous paper,[42] and makes use of the last 50 ps of the trajectory. For the isolated molecule simulations, the starting point of the Brownian dynamics was the equilibrium geometry of each isomer, while for the solvated azobenzene we applied the following equilibration procedure.

We first equilibrated the MM solvent alone, by running 2 ns of molecular dynamics with periodic boundary conditions, constant pressure (1 atm) and temperature (298 K) and 1000 molecules per cell, by means of the MOSCITO package.[83] The final densities of the three solvents agree with the experimental ones (see Table 1). In *n*-hexane the C_2—C_3 bond (or the equivalent C_4—C_5) was found on the average in 80% of the molecules in a *trans* conformation, that is, with the corresponding C—C—C—C dihedral between 150° and 210°; for the central C_3—C_4 bond the *trans* population was 85%; a previous simulation by Thomas et al.[84] yielded 75% and 85% for the two populations, respectively. For MeOH we obtained a good agreement with the experimental $g(R_{OH})$ and $g(R_{OO})$ radial distribution functions[85] (see Figure S1 in Supporting Information). Each molecule was found to be engaged in 1.91 hydrogen bonds, on the average, as evaluated by integrating the first peak in $g(R_{OH})$, up to the distance of the first minimum, R_{OH} = 2.80. The EG results were also compared with those of previous simulations,[79] which were reproduced quite accurately (see Figure S2 in the Supporting Information). In this case, one has to distinguish among the intermolecular H-bonds, which were 3.90 per molecule, on the average, and the intramolecular ones. The latter tend to be longer, because they would close an O—C—C—O—H ring with the consequent bond angle strain. On the average, at least one of the intramolecular R_{OH} distances is shorter than 3 Å in 21.2% of the EG molecules; both distances are below 3 Å in 2.4% of the cases. With the threshold at R_{OH} = 3.5 Å, the two percentages are 45.6% and 24.6%.

Table 1. Physical and Geometrical Parameters of the Solvent Cubic Cells and Spherical Clusters

	n-hexane (HEX)	methanol (MeOH)	ethylene glycol (EG)
computed density (g/cm^3)	0.642	0.761	1.099
experimental density[a] (g/cm^3)	0.655	0.784	1.106
radius of spherical cluster, R_{sph} (Å)	24.0	20.0	22.0
radius of containing wall, R_{wall} (Å)	27.0	21.0	23.0
solvent molecules in the cluster	264	482	481
solvent molecules in the cluster with TAB	258	474	475
solvent molecules. in the cluster with CAB	260	476	473

[a] 1 atm, 298 K.[86]

As a second step, we cut a spherical cluster of solvent molecules from the cubic cell of the previous simulation. All molecules with their centers of mass within R_{sph} from the center of the cubic cell were included. The radii R_{sph} and the numbers of molecules in the clusters are given in Table 1. We also added a confining potential, applied to each atom, to avoid the loss of molecules by evaporation from the cluster surface. The potential has the form

$$V_{conf}(R) = 0 \quad \text{for} \quad R \le R_{wall}$$
$$V_{conf}(R) = \frac{1}{2} K(R - R_{wall})^2 \quad \text{for} \quad R > R_{wall} \qquad (1)$$

Here R is the distance of the atom from the center of the sphere, K = 0.02 au, and R_{wall} is a distance slightly larger than the radius of the cluster (see Table 1).

Next, we carved a cavity in the center of the cluster, by taking out a few solvent molecules, and we replaced them with one azobenzene molecule, either in the *trans* or in the *cis* isomeric form. This step was carried out by an algorithm implemented in the TINKER package.[81] The cluster was further equilibrated by running a Brownian trajectory for about 100 ps, and we used the last 50 ps to sample the initial conditions for the excited state dynamics. In the azobenzene + MeOH and azobenzene + EG clusters, very few solute−solvent hydrogen bonds were established in the average. In fact, no short distance maximum in the radial

dx.doi.org/10.1021/ja1113529 |J. Am. Chem. Soc. 2011, 133, 5109–5123

distribution function $g(R_{NH})$ was observed. To be sure that this was not due to an incomplete equilibration, we ran 20 ps of Brownian dynamics with a larger N···H—O bond strength, by altering the QM/MM parameters, until a small maximum in $g(R_{NH})$ was obtained. However, by restoring the normal bond strength, the maximum disappeared. This is due to the fact, already noted, that the solvent−solvent H-bonds are stronger than the solute−solvent ones.

2.4. Nonadiabatic Dynamics. We applied the "fewest switches" algorithm by Tully,[69] modified with quantum decoherence corrections.[72] We used the time step Δt = 0.1 fs for the integration of the trajectories (Beeman-Verlet method) and for the propagation of the electronic wave functions.[70] Five electronic states (S_0−S_4) were included in the dynamics, to allow for possible transitions from S_1 to the upper states. However, very few upward hops were observed.

The conditions to stop a trajectory were chosen with two aims: to obtain a final structure sufficiently close to the equilibrium geometry of one of the two isomers and to be reasonably sure that no further isomerization events may occur, by hot ground state processes and/or by reverting to the excited states. The backward *cis* → *trans* ground state process had been observed in a previous simulation of TAB photoisomerization, with especially favorable conditions: the azobenzene molecule was subjected to an external force with a destabilizing effect on CAB, and no solvent effects were taken into account.[42] The primary stopping condition is that the azobenzene molecule has reached the electronic ground state. Next, the time elapsed from the excitation must be longer than a threshold t_{min}, to allow for a substantial, although not complete, intra- and intermolecular vibrational energy redistribution among the 66 modes of the azobenzene molecule and from azobenzene to the solvent. On the basis of our previous experience[42] and of the shorter times involved when exciting CAB rather than TAB, we imposed t_{min} = 2.5 ps for a trajectory going from TAB to CAB, 1 ps for a trajectory starting from TAB and reverting to TAB, 1 ps for the CAB → TAB case, and 1.5 ps for the CAB → CAB one. As to the molecular geometry, the stop conditions require that both NNC angles are larger than 150°, to be far from the TS for the N-inversion. Finally, the CNNC dihedral angle must be within ±5° of either 180° or 0°, whereby the product is TAB or CAB, respectively.

3. QUANTUM YIELDS AND EXCITED STATE DYNAMICS

3.1. Quantum Yields. The quantum yield obtained by a simulation starting with the excitation of a given isomer is defined as the fraction of trajectories that are stopped near the equilibrium geometry of the other isomer: these will be called the reactive trajectories, and the others, unreactive. The computed quantum yields are in very good agreement with the experimental data (see Table 2). In vacuo, the present results are quite close to our previous ones.[34] They appear to be affected by the solvent viscosity and much less by its polarity. We recall that the viscosities of *n*-hexane, methanol, and ethylene glycol at 298 K are η = 0.30, 0.54, and 16.1 mPa·s, respectively.[86] In the low viscosity solvents the $\Phi_{t\to c}$ quantum yield is slightly lower than in vacuo, while $\Phi_{c\to t}$ is unaltered. With a higher viscosity, that is, in ethylene glycol, we find a larger $\Phi_{t\to c}$ and a smaller $\Phi_{c\to t}$. This result is not intuitive but is in agreement with the quantum yields measured in another viscous solvent,[2] namely, glycerol at 298 K (η = 934 mPa·s;[86] see again Table 2). Notice that at much higher viscosities (glycerol at 198 K) the $\Phi_{t\to c}$ quantum yield drops to 0.23, more in line with the common expectation that a viscous solvent would hamper any large amplitude internal motion and, particularly, the double bond torsion of ethene, imino, or azo groups with bulky substituents.[2] A simulation of such extreme conditions is planned but faces a major problem as to the equilibration of the azobenzene plus solvent cluster.

Table 2. Photoisomerization Quantum Yields[a]

	$\Phi_{t\to c}$	$\Phi_{c\to t}$
previous work, in vacuo[34]	0.33 ± 0.03	0.61 ± 0.03
this work, in vacuo	0.33 ± 0.02	0.57 ± 0.02
this work, *n*-hexane	0.24 ± 0.02	0.58 ± 0.02
this work, methanol	0.30 ± 0.02	0.57 ± 0.02
this work, ethylene glycol	0.37 ± 0.02	0.49 ± 0.02
experimental, *n*-hexane[4]	0.25	0.56
experimental, methanol[3,5]	0.20−0.28	0.57−0.63
experimental, glycerol (298 K)[2]	0.42	0.53

[a] The statistical standard deviations of the theoretical results, $\Delta\Phi = (\Phi(1-\Phi)/N_{traj})^{1/2}$, are also listed.

3.2. Internal Motions. To understand these trends, we must analyze the reaction mechanism. Figure 2 shows the averages over all the reactive or unreactive trajectories of the most important internal angles and dihedrals that determine the molecular structure, as functions of time. Figure 2 refers to the methanol solution, but essentially the same conclusions can be drawn for the other environments (see Figures S3, S4, and S5 in the Supporting Information). The NNC symmetric bending mode is excited as a consequence of the $n \to \pi^*$ transition, because the loss of one electron from the N lone pairs causes an opening of the NNC angles. In all the figures we show two separate averages, one for the larger and one for the smaller NNC angle. Nevertheless, the two averages almost coincide, that is, the bending motion is strictly symmetric and there is no hint of the single N-inversion that would lead to isomerization. Of course, a short time after excitation the averages of NNC over reactive and unreactive trajectories start diverging, each one approaching the respective final equilibrium value in the ground state. Starting with TAB, one can see several NNC oscillations with a frequency of 155 cm^{-1}, while the torsional motion and the deactivation of CAB in methanol are so fast that only one coherent NNC oscillation can be observed. This is in agreement with the resonant Raman measurements by Stuart et al.,[27] which detect the NNC bending mode of TAB and the CNNC torsion of CAB in ethanol solution. However, we find that the double bond torsion is the most important geometrical change leading to the isomerization and/or to the excited state decay for both the *trans* → *cis* and *cis* → *trans* processes, even in environments where it is slowed down.

Figure 3 shows the time evolution of the averaged CNNC dihedral angle. Before averaging, the angles are all reduced to the [0,180°] range by subtracting 360° and/or changing their sign; otherwise, the averages would be meaningless because of the symmetry of the distributions with respect to 0 and 180°. The initial rate of change of CNNC is the same for all environments, and for both the reactive and unreactive trajectories, up to about 150 fs when the starting isomer is TAB and up to 50 fs when it is CAB (see also the 30° torsion times in Table 3). After these times, the CNNC angle for the unreactive trajectories goes sharply back toward the initial value: as we shall see, this is the result of nonadiabatic transitions to the ground state. The time

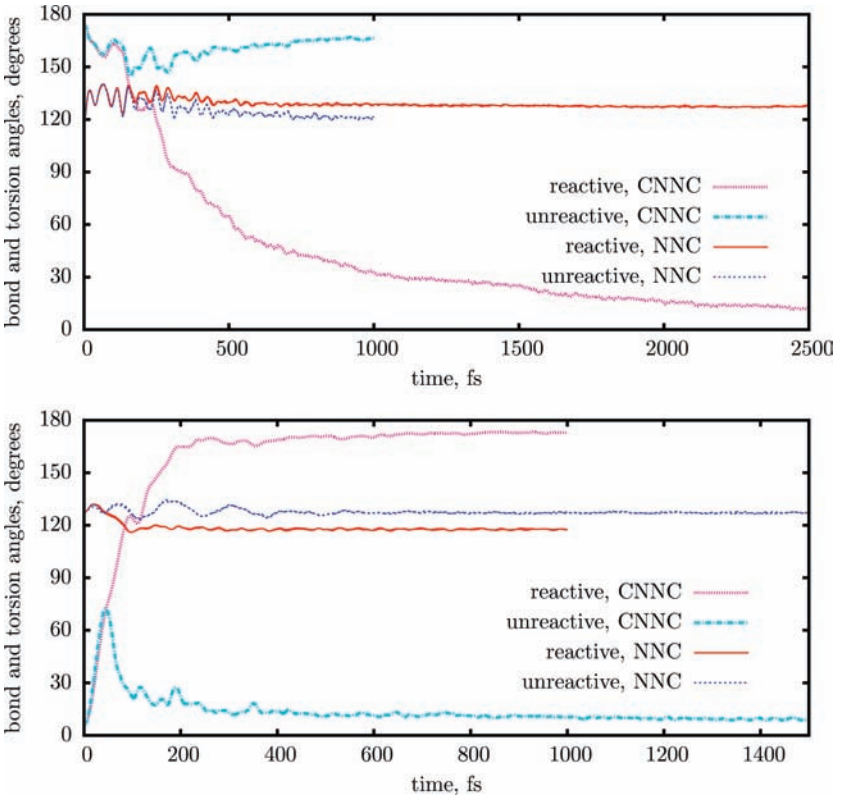

Figure 2. Time dependence of the NNC bond angles and the CNNC dihedral, averaged over the reactive or unreactive trajectories. *trans* → *cis* photoconversion in the upper panel, *cis* → *trans* in the lower panel, both in methanol.

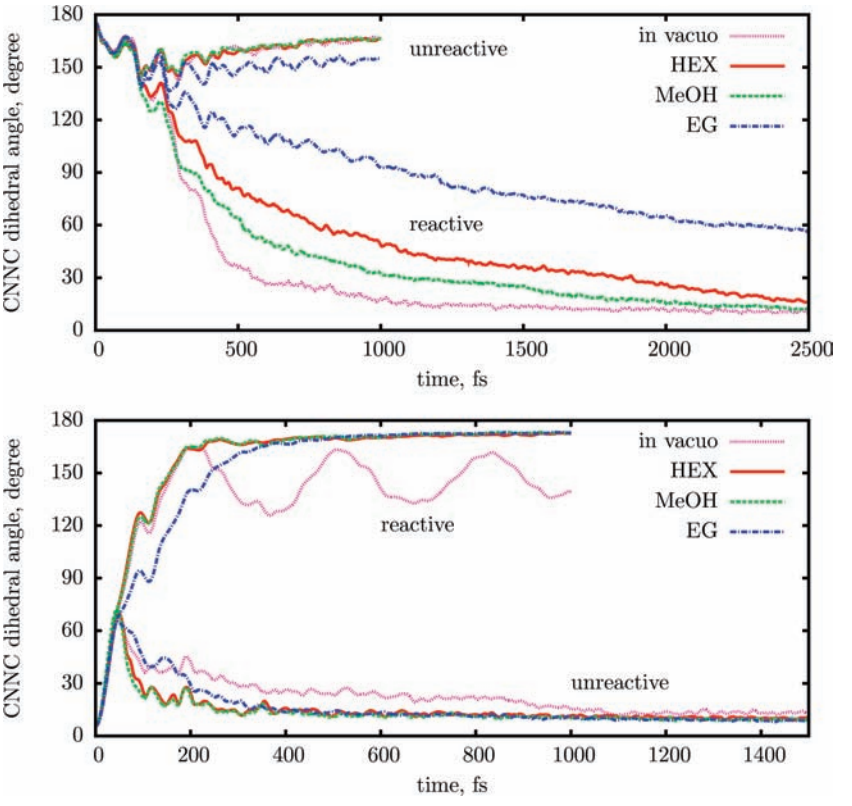

Figure 3. Time dependence of the CNNC dihedral angle, averaged over the reactive or unreactive trajectories, in four different environments. *trans* → *cis* photoconversion in the upper panel, *cis* → *trans* in the lower panel.

dx.doi.org/10.1021/ja1113529 |*J. Am. Chem. Soc.* 2011, 133, 5109–5123

Table 3. Decay Onset Times, Exponential Lifetimes, Weights Obtained by Fitting the S_1 State Populations[a], and 30° Torsion Times $t(\Delta CNNC=30°)$[b] (All Times in ps)

	τ_0	τ_1	τ_2	W_1	$t(\Delta CNNC=30°)$
TAB in vacuo	0.157	0.229		1.00	0.152
TAB in HEX	0.156	0.244	0.92	0.46	0.150
TAB in MeOH	0.127	0.250	0.93	0.58	0.148
TAB in EG	0.162	0.381	2.82	0.23	0.146
CAB in vacuo	0.032	0.038		1.00	0.023
CAB in HEX	0.033	0.032		1.00	0.022
CAB in MeOH	0.032	0.034		1.00	0.021
CAB in EG	0.039	0.096		1.00	0.022

[a] See eq 2; when $W_1 = 1$, one exponential was used. [b] That is, the times by which the average of the CNNC dihedral reaches 150° starting from TAB or 30° starting from CAB.

dependence of CNNC appears to be modulated by the interaction with other skeletal modes; for TAB in ethylene glycol the oscillation with a period of 100 fs is particularly evident. By inspecting the trajectories of TAB one by one, one finds that CNNC remains confined for a while in the transoid region (roughly CNNC > 130°); then, in the reactive case, a fast transition toward small CNNC angles takes place in 20−30 fs (see Figures S8 and S9 in the Supporting Information). This means that the averages depicted in Figure 3 combine the contributions of trajectories at transoid geometries with those already at cisoid geometries, the balance shifting gradually in time toward the latter. The delay of the isomerization depends on the environment: it is fastest in vacuo and slowest in EG. Methanol and *n*-hexane yield similar results, but the latter, although less viscous, has a slightly larger slowing effect: this is a clue that the large differences in the size and mass of the solvent molecules in this case are more important than the intermolecular interactions and solvent structure. In fact, Malhado et al. have recently emphasized the importance of solvent relaxation times (that are related to molecular masses and sizes), in modeling a photoisomerization in condensed phase.[87] The slowing down correlated with the solvent properties is much more evident in the *trans* → *cis* process than in the *cis* → *trans* one, because on the CAB side the slope of the PES is larger and drives more forcefully the motion along the torsional coordinate. In vacuo, the *cis* → *trans* torsion acquires a sufficiently large momentum as to give place to oscillations around the TAB minimum, but in all the solvents this motion is efficiently damped out (such oscillations are centered around CNNC = 180°, but in our plot they range from ∼130° to ∼160° because of the reduction to the interval [0,180°] applied when averaging CNNC).

As expected for any considerable geometrical rearrangement, the double bond torsion is coordinated with other internal motions, in order to minimize the overall displacement of atoms. This occurs in vacuo, due to inertial effects, and even more in the condensed phase, because the surrounding molecules hinder any large amplitude motion. In azobenzene, the reorientation of each phenyl group and of the inertial axes of the whole molecule is minimized by coordinating the N═N bond torsion with a simultaneous torsion of the N—C bonds. This behavior was already observed by Ootani et al., who performed a full simulation of the $n \rightarrow \pi^*$ *cis* → *trans* and *trans* → *cis* photodynamics with CASSCF/STO-3G PES for the isolated molecule and by Böckmann et al., who ran a few trajectories starting from CAB[88] and from TAB[89] in pure liquid azobenzene, with a QM/MM approach based on DFT. Instead of flapping the phenyl rings, this "pedalling" motion modifies the orientation of the N—N axis. Thanks to this mechanism, the negative influence of the solvent viscosity on the N═N torsion and on the quantum yields is effectively reduced. In Figure 4 we show how the phenyl groups reorient themselves in the four different media. We consider the vector $\vec{V}_i$ $(i = 1,2)$ perpendicular to each phenyl ring, identified as the principal axis of the six carbon atoms with the largest moment of inertia; then, for each trajectory, we compute the rotation underwent by the phenyl ring as the angle $\alpha_i(t)$ between $\vec{V}_i(t)$ and the initial direction $\vec{V}_i(0)$. In Figure 4 we plot the averages over all reactive or unreactive trajectories of $(\alpha_1(t) + \alpha_2(t))/2$. The plots show that in solution the phenyl rings are less free to reorient themselves than in vacuo, and EG is the most constraining solvent of the three. This trend is quite apparent at long times, for both isomers, but a comparison can also be made at some equivalent point along the reaction pathway. To this aim, we have marked with arrows the midpoint of the pathway, that is, the time when the CNNC angle, averaged over the reactive trajectories, is 90. For CAB excitation, we hardly find a difference between the four media at the midpoint of the pathway, which is reached very soon (60−80 fs), with little displacement of the phenyl rings. For TAB, at the same stage the rotation of the phenyl rings is smaller in EG than in the other media, in spite of the much longer time elapsed.

3.3. Excited State Decay. Figure 5 shows the time dependence of the excited state population, that is, the fraction of trajectories running on the S_1 PES at a given time. The S_1 decay curves are characterized by an onset time τ_0, during which almost no loss of population occurs; after τ_0 they can be fitted by a biexponential form:

$$\begin{aligned} P_1(t) &= 1 && \text{for} \quad t \le \tau_0 \\ P_1(t) &= W_1 e^{-(t-\tau_0)/\tau_1} (1 - W_1) e^{-(t-\tau_0)/\tau_2} && \text{for} \quad t \ge \tau_0 \end{aligned} \tag{2}$$

The onset times, lifetimes, and weights are given in Table 3. It turns out that two exponentials are needed only for TAB in solution, where the second component has lifetimes in the picosecond range. The onset times of TAB are close to the 30° torsion times, and those of CAB are a little larger. It is apparent that the $S_1 \rightarrow S_0$ transition is slowed down, depending on the solvent properties, in much the same way as the torsional motion.

The relationship between nonadiabatic events (i.e., surface hops) and geometrical relaxation is further clarified by the data shown in Table 4 and in Figure 6. Most trajectories only undergo one hop, from S_1 to S_0, but a minority (up to 22%, the highest fraction being found in vacuo) hop back to the S_1 state and again to S_0 later on. The averaged CNNC angles at the time of the S_1-S_0 hops, listed in Table 4, in all cases fall short of the midpoint of the reaction path, which corresponds to the TS for the torsional pathway, at CNNC ≃ 90°; however, the reactive trajectories hop to S_0 closer to the TS than the unreactive ones. This difference is more marked for the *trans* → *cis* than for the *cis* → *trans* conversion; in the *trans* → *cis* case also the $\Delta U(S_0-S_1)$ energy gap is consistently smaller in the reactive trajectories; that is, the hops occur closer to the crossing seam. These data confirm that the quantum yields are determined by a competition between the progress along the reaction coordinate and the

dx.doi.org/10.1021/ja1113529 |*J. Am. Chem. Soc.* 2011, 133, 5109–5123

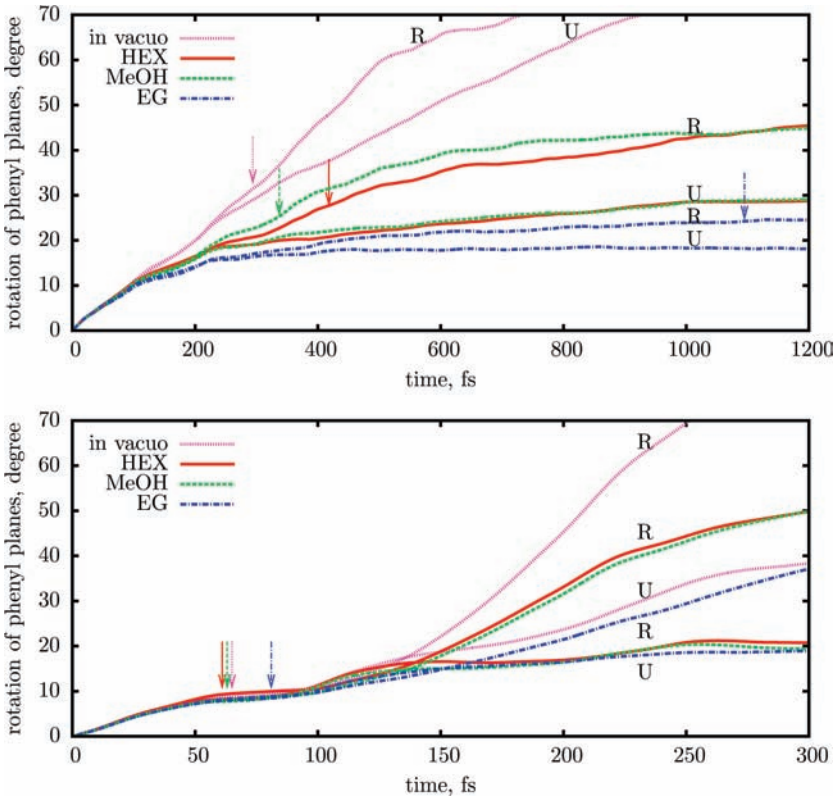

Figure 4. Rotation angles of the phenyl groups, averaged over the reactive and the unreactive trajectories, are marked with "R" and "U", respectively. The arrows mark the midpoint of the reactive trajectories, i.e., the time when the average of the CNNC torsion angle is 90°. *trans* → *cis* photoconversion in the upper panel, *cis* → *trans* in the lower panel.

nonadiabatic decay. If a molecule switches to S_0 when it is still far from the TS, most of the time it goes back to the starting isomer. At such geometries the S_0-S_1 gap is large; therefore, a strong nonadiabatic coupling is needed, which means a large projection of the nuclear velocities along the dynamic coupling vector $\langle\psi_0|(\partial/\partial Q)|\psi_1\rangle$. Since the latter mainly involves the azo group where the excitation is localized, in Figure 6 we show the correlation between $\Delta U(S_0-S_1)$ and the kinetic energy of the azo atoms C—N═N—C (T_{CNNC}), for the *trans* → *cis* photoconversion. In all cases, most hops crowd at small $\Delta U(S_0-S_1)$, with CNNC between 95° and 110° and T_{CNNC} between 0.1 and 0.4 eV. In vacuo and with *n*-hexane or methanol as solvents, a consistent fraction of the hops ("early hops") occur at larger values of CNNC, $\Delta U(S_0-S_1)$ and T_{CNNC}, and most of them belong to unreactive trajectories (see Figure S6 in the Supporting Information for the in vacuo and HEX cases). In ethylene glycol, the early hops are almost completely suppressed, because the N═N bond torsion is delayed and there is time to transfer part of the vibrational energy from the azo group to the rest of the molecule and to the solvent. In this way all hops must occur closer to the TS in S_0, and this is why the quantum yield is higher in ethylene glycol. The nuclear velocity factor in the nonadiabatic coupling was neglected in the simulations run by Tiberio et al.,[47] as they assumed the transition rate to depend on $\Delta U(S_0-S_1)$ only; as a result, their computed quantum yield in EG is smaller than in the less viscous solvents, which can be taken as a further test of the importance of such dynamical effects on the transition rates. The role of nonadiabatic events taking place far from the crossing seam is well analyzed in the model simulations of a photoisomerization, run by Malhado et al.[87]

4. FLUORESCENCE EMISSION SIMULATION

Among the most revealing experiments on azobenzene photodynamics are the measurements of time-resolved fluorescence of TAB in two solvents of different viscosity by Chang et al.[25] Emission intensities $I_{\parallel}(t)$ and $I_{\perp}(t)$, with polarization respectively parallel and perpendicular to that of the exciting light, were recorded as functions of the pump−probe delay by the fluorescence up-conversion technique. The ratio $I_{\perp}/I_{\parallel}$, as well as the more commonly used anisotropy ratio $R = (I_{\parallel} - I_{\perp})/(I_{\parallel} + 2I_{\perp})$, depends on the angle between the transition dipole vector for photon emission and that for the absorption. With parallel dipoles, which is the limiting case immediately after excitation, one gets $R = 2/5$, while two perpendicular dipoles yield $R = -1/5$. If the same pair of electronic states is involved in absorption and emission, as in the present case, only the geometrical relaxation and the overall molecular rotation can change the direction of the transition dipole, so the measurement of $R(t)$ may yield valuable information about these processes.

Chang et al.[25] found that the decay of the fluorescence intensity is slower in ethylene glycol than in *n*-hexane, by roughly a factor two, while the fluorescence anisotropy is dramatically affected by solvent viscosity. The anisotropy ratio $R(t)$ in HEX decreases from the initial value of 0.4 to 0.3 in 1.5−2 ps and to 0.25 in about 3 ps; at later times, given the weakness of the signal, the uncertainty is very high. In EG, $R(t)$ remains almost unchanged during the whole time interval in which it can be reliably measured, save that it decreases slightly during the first 1−2 ps, to values of 0.36−0.38. On the basis of these results, the authors suggested that the torsional mechanism, supposedly more effective in causing depolarization, is essentially

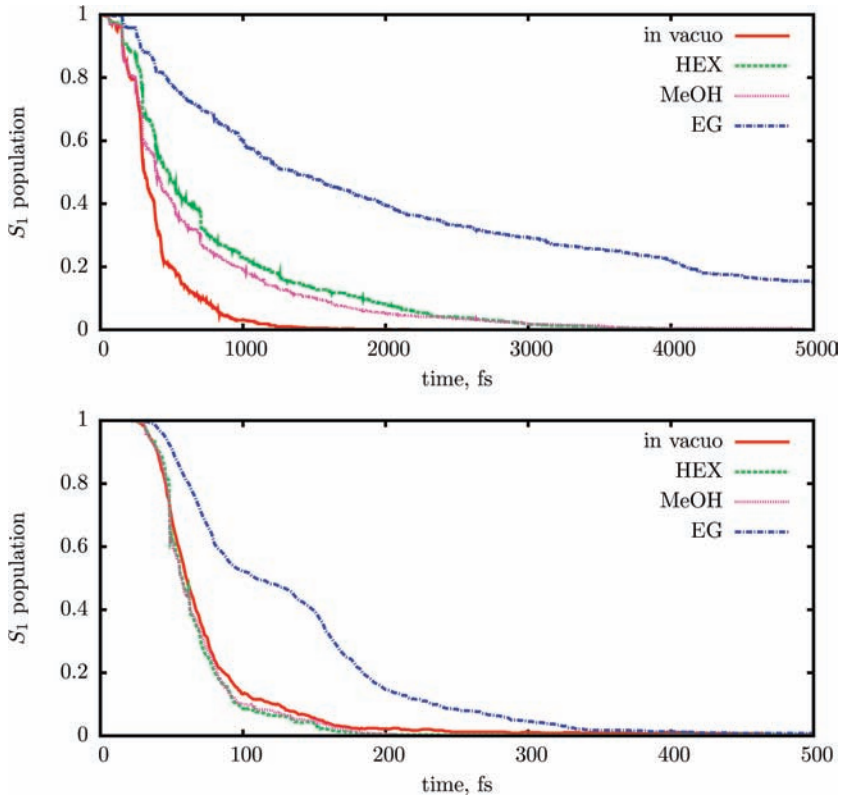

Figure 5. Time dependent population of the S_1 state in four different environments. *trans* → *cis* photoconversion in the upper panel, *cis* → *trans* in the lower panel.

Table 4. Dynamical Quantities at the Time of the Nonadiabatic Hops from S_1 to S_0[a]

trans → *cis*		CNNC	T_{CNNC}[b]	ΔU[c]
in vacuo	reactive	103 ± 8	0.328 ± 0.107	0.086 ± 0.123
	unreactive	112 ± 14	0.313 ± 0.122	0.196 ± 0.300
n-hexane	reactive	104 ± 5	0.287 ± 0.104	0.058 ± 0.056
	unreactive	113 ± 13	0.304 ± 0.139	0.212 ± 0.305
methanol	reactive	104 ± 6	0.301 ± 0.105	0.065 ± 0.088
	unreactive	113 ± 11	0.288 ± 0.119	0.192 ± 0.268
ethylene glycol	reactive	103 ± 5	0.237 ± 0.092	0.035 ± 0.032
	unreactive	106 ± 8	0.245 ± 0.102	0.067 ± 0.149
cis → *trans*		CNNC	T_{CNNC}[b]	ΔU[c]
in vacuo	reactive	82 ± 6	0.371 ± 0.128	0.104 ± 0.087
	unreactive	81 ± 5	0.336 ± 0.115	0.089 ± 0.109
n-hexane	reactive	82 ± 4	0.389 ± 0.137	0.113 ± 0.090
	unreactive	81 ± 5	0.359 ± 0.128	0.113 ± 0.092
methanol	reactive	82 ± 5	0.375 ± 0.131	0.098 ± 0.080
	unreactive	81 ± 4	0.338 ± 0.108	0.102 ± 0.089
ethylene glycol	reactive	84 ± 6	0.335 ± 0.125	0.054 ± 0.047
	unreactive	83 ± 6	0.317 ± 0.119	0.048 ± 0.048

[a] All quantities are averaged over the reactive or unreactive trajectories. Standard deviations are also given. [b] Nuclear kinetic energy of the azo CNNC atoms (eV). [c] S_0-S_1 energy gap (eV).

suppressed in viscous solvents. Since our simulations show that the isomerization occurs by torsion in EG too, we have computed the fluorescence transients in order to validate our results and offer an alternative interpretation of the experimental findings.

4.1. Steady State Spectra and Time-Dependent Intensities. The photon emission rate averaged over all trajectories is

$$I_{tot}(t) = \frac{4}{3N_T\hbar^4c^3}\sum_{k=1}^{N_T}\left[\sum_{I=0}^{J-1}\Delta U_{IJ}{}^3\mu_{IJ}{}^2\right]^{(k)} \quad (3)$$

Here N_T is the total number of trajectories, and all the quantities in square brackets depend on time and on the trajectory index k: J is the current state for trajectory k at time t, while ΔU_{IJ} and μ_{IJ} are the relevant transition energy and dipole moment. Since the trajectories very seldom hop to higher excited states, the fluorescence is almost exclusively due to $S_1 \rightarrow S_0$ transitions. By partitioning the sum 3 according to intervals of $\lambda_{flu}=hc/\Delta U_{IJ}$, one gets the time dependent emission spectrum $I(\lambda_{flu},t)$. The corresponding steady state spectrum (photon emission differential cross section as a function of wavelength, in nm^{-1}) is obtained by integrating over time:

$$I(\lambda_{flu}) = \int_0^\infty I(\lambda_{flu},t)\,dt \quad (4)$$

The fluorescence quantum yield is given by

$$\Phi_F = \int_0^\infty I_{tot}(t)\,dt = \int_0^\infty I(\lambda_{flu})\,d\lambda_{flu} \quad (5)$$

In eq 3 one can also select the excitation wavelength $\lambda_{exc} = hc/\Delta E_{exc}$, thus producing the transients $I(\lambda_{exc},\lambda_{flu},t)$ that are measured in fluorescence up-conversion experiments.

The computed steady state fluorescence spectra of TAB feature a broad band, extending roughly from 500 to 1200 nm, with λ_{max} between 650 and 740 nm, depending on the environment; for CAB, the maximum is around 460 nm, with a long tail

dx.doi.org/10.1021/ja1113529 |*J. Am. Chem. Soc.* 2011, 133, 5109–5123

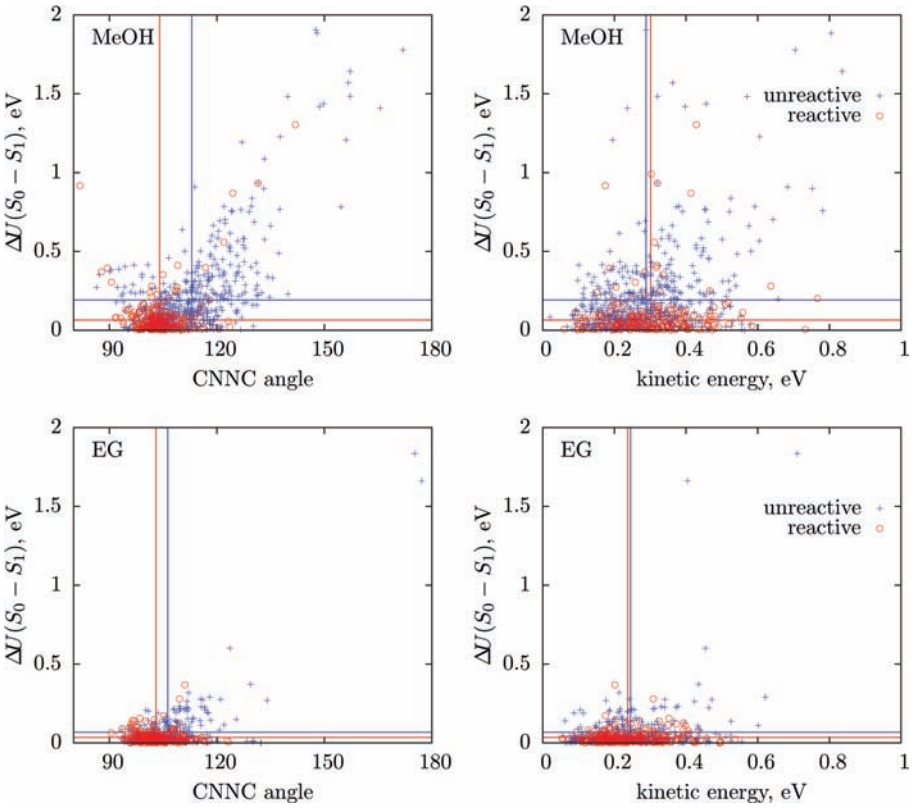

Figure 6. $\Delta U(S_0-S_1)$ energy gap at the time of the $S_1 \rightarrow S_0$ hops, as a function of the CNNC dihedral angle and of the kinetic energy T_{CNNC} of the azo CNNC atoms, for the *trans* → *cis* photoconversion in methanol and ethylene glycol. The straight lines indicate the averages of $\Delta U(S_0-S_1)$, CNNC, and T_{CNNC}.

Table 5. Fluorescence Quantum Yields Φ_F and Maximum Intensity Wavelengths λ_{max} (nm)

	TAB		CAB	
	$\Phi_F \times 10^6$	λ_{max}	$\Phi_F \times 10^6$	λ_{max}
calc. in vacuo	1.04	650	0.19	455
calc. in HEX	2.14	670	0.17	460
calc. in MeOH	1.80	685	0.18	460
calc. in EG	9.56	740	0.26	460
exp. in DMSO, λ_{exc} = 488 nm[23]	3.2	640	0.5	600
exp. in ethanol, λ_{exc} = 458 nm[27]	11	530	1	520

on the long wavelength side. The essential results are collected in Table 5, along with the experimental data by Satzger et al.[23] and Stuart et al.[27] (see also Figure S7 in the Supporting Information). We note that recording the very weak fluorescence of azobenzene is not easy and entails some operations that may give place to rather large errors, such as the subtraction of the solvent background and, in the case of CAB, of the residual TAB contribution. This may explain part of the discrepancies between the two sets of experimental data and with the theoretical results. The computed fluorescence quantum yields Φ_F are much larger in TAB than in CAB (TAB/CAB ratios ranging from 5 to 36); in the case of TAB, we find a marked increase along the sequence: gas phase − HEX and MeOH − EG. The Stokes shift is also larger and more affected by the environment for the TAB isomer. These features are related to the longer lifetime of TAB, but a full explanation requires a more detailed analysis of the dynamical effects.

In Figure 7 we plot the computed fluorescence intensity $I_{tot}(t)$, as a function of time, for the TAB isomer. The raw data are shown for the HEX solution only, for better clarity. They exhibit very wide and fast oscillations, with the same frequency in all solvents (115 cm^{-1}). This frequency coincides with that of the symmetric NNC vibration and each minimum of $I_{tot}(t)$ corresponds to the maximum opening of the angles, where the ΔU_{IJ}^3 factor in the emission rate assumes its lowest value. Such oscillations were not detected by the fluorescence up-conversion measurements because their period (46 fs) is much shorter than the instrumental time resolution.[25] Therefore, we have convoluted our $I_{tot}(t)$ results with a Gaussian function:

$$I_{conv}(t) = \int_{-\infty}^{t} I_{tot}(t-t')\, g(t')\, dt' = \int_{0}^{\infty} I_{tot}(t'')\, g(t-t'')\, dt'' \qquad (6)$$

where $g(t)$ is a normalized Gaussian with fwhm ≃ 200 fs, which is the experimental time resolution[25] (the exact value of the fwhm depends on λ_{exc} and λ_{flu}). The $I_{conv}(t)$ curves are much more similar to the experimental ones. For a more accurate comparison, we also computed $I_{conv}(t)$ for specific pump and probe wavelengths, that is, by using $I(\lambda_{exc},\lambda_{flu},t)$ in place of $I_{tot}(t)$. In Figure 8 we show the simulated and experimental results for λ_{exc} = 440 nm and λ_{flu} = 680 nm. The agreement is quite good, the most noticeable difference being found in the long time tail of the HEX emission, which is slightly underestimated by our simulation.

dx.doi.org/10.1021/ja1113529 |*J. Am. Chem. Soc.* 2011, 133, 5109–5123

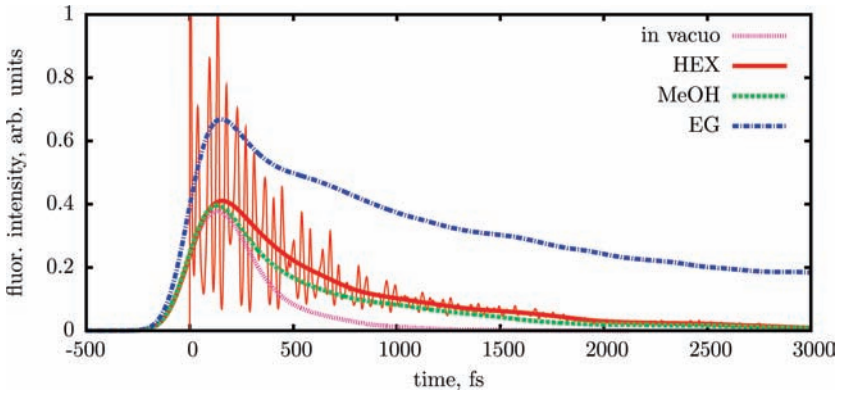

Figure 7. Simulated time-resolved fluorescence of TAB in vacuo and in the three solvents. The oscillatory curve refers to the nonconvoluted signal (in HEX); the others are convoluted with a Gaussian function (fwhm = 200 fs).

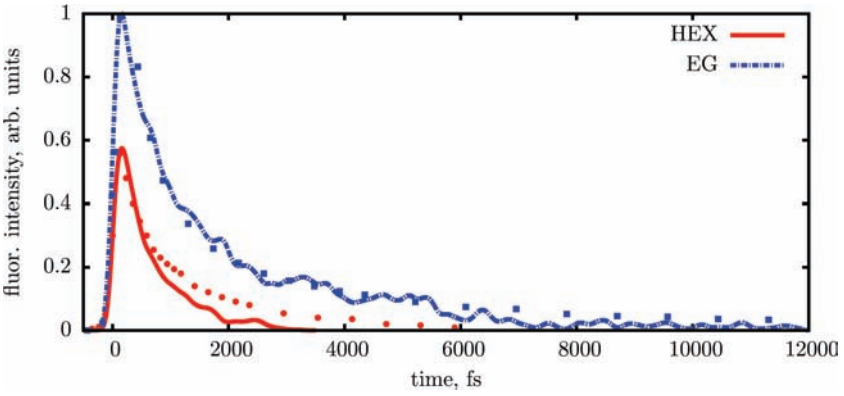

Figure 8. Simulated time-resolved fluorescence of TAB in HEX and EG, with $\lambda_{exc} = 440 \pm 20$ nm and $\lambda_{flu} = 680 \pm 40$ nm. Convolution times: $\tau_c = 190$ fs for HEX and 210 fs for EG. The dots represent experimental data in HEX, the squares in EG.

The $I_{conv}(t)$ data can be fitted very accurately by assuming a biexponential decay: $I_{tot}(t) = W_1 e^{-t/\tau_1} + W_2 e^{-t/\tau_2}$, and analogously for $I(\lambda_{exc},\lambda_{flu},t)$. The lifetimes τ_1 and τ_2 and the weight ratio W_2/W_1 are shown in Table 6. Only the emission of the isolated molecule is well fitted by a single exponential, thus confirming that the longer lifetime component is a solvent effect. Our fitting scheme differs from the more complex one Chang et al.[25] adopted on the basis of mechanistic assumptions that are partly at variance with our findings. Therefore, the lifetimes we find are not strictly comparable with theirs but are of the same order of magnitude. We also reproduce the trends toward longer lifetimes that are observed by increasing the probe wavelength λ_{flu} or by replacing HEX with EG.

4.2. Fluorescence Anisotropy. The most striking effect of solvent viscosity is the almost complete suppression of fluorescence depolarization. To compute the parallel and perpendicular components of the fluorescence emission, eq 3 is modified

$$I_{\parallel,\mathrm{tot}(t)} = \frac{4}{15N_T\hbar^4c^3}\sum_{k=1}^{N_T}\left[\sum_{I=0}^{J-1}\Delta U_{IJ}{}^3\mu_{IJ}{}^2(1+2\cos^2\beta_{IJ})\right]^{(k)} \quad (7)$$

$$I_{\perp,\mathrm{tot}(t)} = \frac{4}{15N_T\hbar^4c^3}\sum_{k=1}^{N_T}\left[\sum_{I=0}^{J-1}\Delta U_{IJ}{}^3\mu_{IJ}{}^2(2-\cos^2\beta_{IJ})\right]^{(k)} \quad (8)$$

Table 6. Exponential Lifetimes and Weights Obtained by Fitting Computed Fluorescence Intensities and Anisotropies of TAB[a]

	λ_{exc}	λ_{flu}	τ_1	τ_2	W_2/W_1	τ_R	$R(\infty)$
in vacuo			0.26		0.00		
in HEX			0.44	1.13	0.39	2.52	0.26
in HEX	440 ± 20	520 ± 40	0.21	0.78	0.05	1.32	0.28
in HEX	440 ± 20	600 ± 40	0.38	1.67	0.05	1.73	0.25
in HEX	440 ± 20	680 ± 40	0.54	1.01	0.28	1.37	0.31
in MeOH			0.24	0.92	0.50	0.80	0.34
in EG			0.32	2.84	1.51	0.22	0.385
in EG	440 ± 20	680 ± 40	0.57	2.85	0.57	0.22	0.386

[a] Data not associated with specific λ_{exc} and λ_{flu} ranges refer to the total emission I_{tot} computed for the whole swarm of trajectories (all excitation energies). Times in ps and wavelengths in nm.

Here $\beta_{IJ}(t)$ is the angle between the $\vec{\mu}_{01}$ transition dipole at time $t = 0$ and $\vec{\mu}_{IJ}(t)$, for the kth trajectory.

The computed anisotropy as a function of time is shown in Figure 9. As in the fluorescence up-conversion measurements, the $R(t)$ curve becomes increasingly erratic as the emission intensity tends to vanish. In EG, an asymptotic value $R(\infty)$ is clearly reached before the data become unreliable; as pointed out by Chang et al.,[25] the rotational depolarization should be negligible in the ps time scale, so the initial decrease and the

dx.doi.org/10.1021/ja1113529 |J. Am. Chem. Soc. 2011, 133, 5109–5123

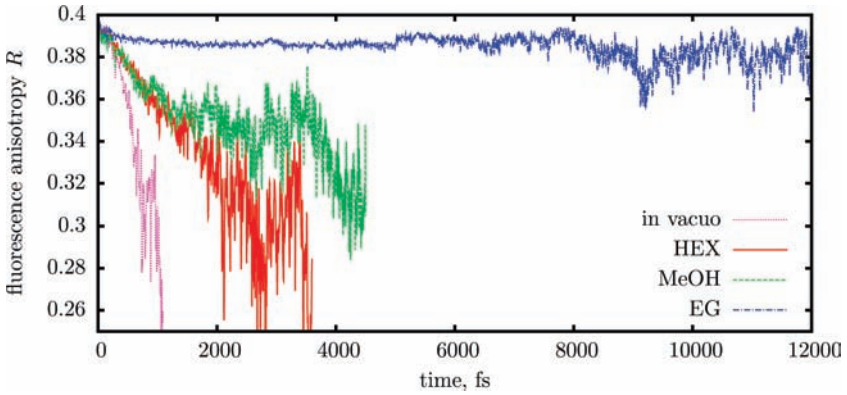

Figure 9. Simulated time-resolved fluorescence anisotropy of TAB in vacuo and in the three solvents.

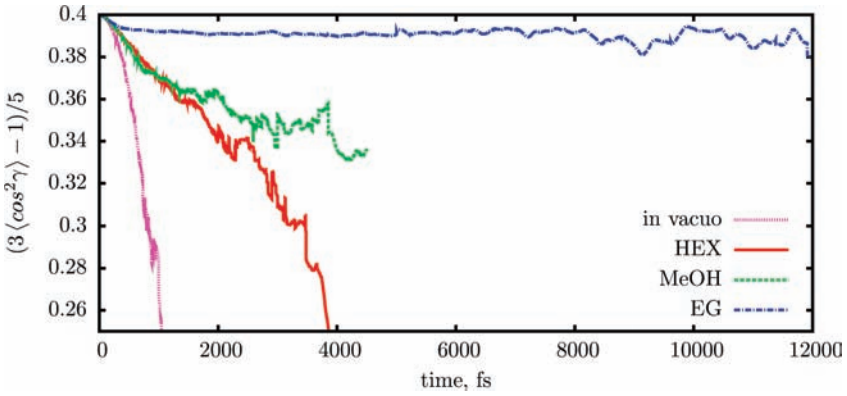

Figure 10. Depolarization of the long principal axis of TAB, $\vec{X}_{pa}$, computed as the average of the function $(3\cos^2\gamma - 1)/5$; here $\gamma(t)$ is the angle between $\vec{X}_{pa}$ at time t and at the excitation time ($t = 0$) for trajectory k, and the average is taken over all trajectories running on the S_1 PES.

asymptotic value are only due to the photodynamics. The anisotropy data are therefore well fitted by the simple function:

$$R_{tot}(t) = R(\infty) + \left[\frac{2}{5} - R(\infty)\right] e^{-t/\tau_R} \qquad (9)$$

Although the asymptotic limit $R(\infty)$ is not so well-defined in HEX or MeOH, the same formula can be used also in these cases. In vacuo, the depolarization is faster and not exponential. The τ_R and $R(\infty)$ parameters are given in Table 6. The initial depolarization rate is roughly the same in the three solvents: $(dR/dt)_{t=0} = [R(\infty) - 0.4]/\tau_R$ takes the values −0.056, −0.075, and −0.068 ps^{-1} in HEX, MeOH, and EG, respectively. However, in EG the depolarization stops much earlier; that is, τ_R is smaller and $R(\infty)$ is closer to the maximum theoretical value $R = 2/5$.

To interpret these findings, we must consider the effect of the molecular motions on the direction of the S_0-S_1 transition dipole $\vec{\mu}_{01}$. At the C_{2h} equilibrium geometry of TAB, $\vec{\mu}_{01}$ vanishes, but a previous ab initio study[41] showed that out-of-plane deformations, such as the N—C or N═N bond torsions, are quite effective in mixing the $n \rightarrow \pi^*$ (S_1) and $\pi \rightarrow \pi^*$ (mainly S_2) states. This is why the S_0-S_1 transition features a small oscillator strength ($f \simeq 0.01$). At all the relevant geometries, $\vec{\mu}_{01}$ is essentially parallel to the transition dipole of the S_0-S_2 transition; it makes a remarkably constant angle α of about 53° with the N—N axis and is perpendicular to the C_2 axis of the C—N═N—C group. The semiempirical calculations reproduce quite well these data and yield $\alpha \simeq 45°$. In practice, the direction of $\vec{\mu}_{01}$ coincides with the long axis of inertia of TAB.

Another important element to be considered is that most of the TAB fluorescence is emitted when the C—N═N—C group is not too far from planarity: the fraction of the total emission with CNNC > 150° is 61% in HEX and 52% in EG; with CNNC > 135° we get 92% and 86%, respectively. This happens because the torsion of the double bond is fast, in comparison with the time spent at transoid geometries, as already observed in Section 3.2 (see Figures S8 and S9 in the Supporting Information).

Both the double bond torsion (as discussed in Section 3.2) and the symmetric NNC bending motion may cause a change in the orientation of the N—N axis and of the $\vec{\mu}_{01}$ vector. The effect on the fluorescence depolarization is small, because of the limited range of variation of these internal coordinates in the excited state, and because any geometrical change that brings the S_1 and S_0 PESs closer to each other decreases the photon emission rate and increases the radiationless decay rate (the dependence of the emission intensity on the NNC bending is apparent in the nonconvoluted plot of Figure 7).

The internal motions, however, can also be associated with an overall rotation of the molecule, as far as the solvent cage allows. The cage itself can be loosened thanks to the partial conversion of the photon energy into vibrational excitation, which is then transferred to the solvent. The reorientation process will rapidly slow down and terminate once the chromophore and the surrounding solvent molecules have thermalized (the slower ground state rotational diffusion that follows does not concern

dx.doi.org/10.1021/ja1113529 |J. Am. Chem. Soc. 2011, 133, 5109–5123

us in this context). To monitor the effect on the reorientation of the transition dipole vector, which is roughly parallel to the long axis of TAB, we considered the principal axis of inertia with the smallest moment, $\vec{X}_{pa}$. As a proxy of the β_{01} angle of eqs 7 and 8 we took the change in the orientation of $\vec{X}_{pa}$, that is, the angle γ between $\vec{X}_{pa}(t)$ and its initial direction $\vec{X}_{pa}(0)$. By putting γ instead of β_{01} in eqs 7 and 8 and neglecting the weights ${U_{01}}^3{\mu_{01}}^2$ in the averaging, the anisotropy ratio R is replaced by $R_{pa}(t) = (3\langle\cos^2\gamma\rangle - 1)/5$. The $R_{pa}(t)$ curves, shown in Figure 10, closely parallel those of the fluorescence anisotropy $R(t)$, apart from two details: they are less noisy, because they are much less affected by the fast vibrations, and they have a smaller initial slope, ≈ -0.02 ps^{-1} instead of ≈ -0.06 ps^{-1}. The $R_{pa}(t)$ functions remain less steep than $R(t)$ for about 0.5 ps, so that at later times for each solvent R_{pa} is slightly larger than R. This difference is due to the internal motions, which cause a fast but small depolarization, about the same in all environments. The main difference between the three solvents is due to the overall rotation of TAB, which is almost absent in ethylene glycol.

5. CONCLUSIONS

We have performed a set of simulations of the photodynamics of *trans*- and *cis*-azobenzene in different environments: in vacuo, in *n*-hexane, in methanol, and in ethylene glycol. The simulation procedure was not calibrated versus empirical results; only the semiempirical method by which we compute the PES and the electronic wave functions has been reparameterized to fit the best ab initio, spectroscopic, and thermochemical data.

The simulations reproduced well the measured quantum yields for the *trans* → *cis* and *cis* → *trans* photoconversions, and in particular the increasing trend of $\Phi_{t\rightarrow c}$ with solvent viscosity. This feature is due to the intra- and intermolecular vibrational energy redistribution occurring in the S_1 state, which proceeds to a greater extent in viscous solvents where the molecule remains for much longer times at transoid geometries. With smaller vibrational energies the nonadiabatic transitions are less effective, and a larger fraction of molecules must approach the crossing seam between S_0 and S_1 before they can decay to the ground state. In this way, they get closer to the transition state for the torsion around the N═N double bond, thus increasing the isomerization probability.

The reaction coordinate is essentially the N═N torsion for both the *trans* → *cis* and *cis* → *trans* processes and in all environments. The torsion is assisted by simultaneous rotations of the C—N bonds, such as to minimize the reorientation of the phenyl groups, especially (but not only) in the condensed phase. When the *trans* isomer absorbs a photon, the NNC symmetric bending vibration is excited, as already predicted by us on the basis of simulations for the isolated molecule[34] and detected by Stuart et al. with resonant Raman scattering. However, the NNC bending does not lead to isomerization: in fact, it rather facilitates the excited state decay. The molecule remains at transoid geometries during a time that falls in the picosecond range and increases with solvent viscosity; then, a fast torsion takes place in 20−30 fs, leading to a nonadiabatic transition to the ground state and possibly to the isomerization. The *cis* isomer undergoes a much prompter N═N torsion and faster nonadiabatic decay than the *trans* one, because of the steeper slope of the PES on the *cis* side. For the same reason, the excited state dynamics and the quantum yields are more influenced by the environment when starting from the *trans* isomer than from the *cis* one.

Chang et al.[25] measured quite different fluorescence transients for *trans*-azobenzene in *n*-hexane and in ethylene glycol. In the more viscous solvent the lifetimes are roughly twice as long as in the former one. More strikingly, the fluorescence depolarization is almost completely suppressed in ethylene glycol during at least 10 ps, while it proceeds to a considerable extent in *n*-hexane within 2−3 ps. These differences led the authors to propose a solvent induced change in the reaction and decay mechanism. Our simulated time-dependent emission intensities and anisotropies agree very well with the experimental ones, but they can be interpreted within the torsional mechanism, with a small contribution of the NNC symmetric bending to the initial depolarization. The solvent effect on the depolarization is almost entirely explained by the overall rotation of the chromophore, which is much more pronounced in the less viscous and associated solvent.

In all solvents, most of the fluorescence is emitted when *trans*-azobenzene is still at transoid geometries, that is *before* the fast N═N torsional motion that leads to the S_0-S_1 crossing seam and transition state region. As a consequence, it is difficult to obtain clues about the photoisomerization mechanism from the fluorescence transients, and the same holds for the resonant Raman spectra. At present, computational simulations with the necessary validation against the experimental results seem to be the best way to extend our knowledge to the crucial events of the azobenzene photodynamics, that is, the $S_1 \rightarrow S_0$ nonadiabatic transition and the crossing of the transition state. Indirect clues can be obtained from the dependence of the quantum yields on solvent viscosity, about which more complete sets of data would be welcome. To probe the crucial part of the dynamics it is not sufficient to improve the time resolution of the transient measurements, because there is no well-defined time delay at which such events take place. Our suggestion is to rely on the selectivity (based on geometrical, electronic, or spectral properties) of pump-and-probe methods such as time-resolved photoelectron spectroscopy or pulsed X-rays.

■ ASSOCIATED CONTENT

Supporting Information. Semiempirical method and parameters and additional figures. This material is available free of charge via the Internet at http://pubs.acs.org.

■ AUTHOR INFORMATION

Corresponding Author
mau@dcci.unipi.it

■ ACKNOWLEDGMENT

This work was supported by grants from the Italian MIUR (PRIN Project 2006030944) and of the University of Pisa. A generous allocation of computer time was provided through TeraGrid resources by NCSA under Grant Number TG-CHE090047. We are grateful to Dr. Giacomo Prampolini for his advice about MD simulations. This paper is dedicated to the memory of Alberto Marini.

■ REFERENCES

(1) Zimmermann, G.; Chow, L.-Y.; Paik, U.-J. *J. Am. Chem. Soc.* **1958**, *80*, 3528.
(2) Gegiou, D.; Muszkat, K. A.; Fischer, E. *J. Am. Chem. Soc.* **1968**, *90*, 12.

(3) Ronayette, J.; Arnaud, R.; Lebourgeois, P.; Lemaire, J. *Can. J. Chem.* **1974**, *52*, 1848.
(4) Bortolus, P.; Monti, S. *J. Phys. Chem.* **1979**, *83*, 648.
(5) Gauglitz, G.; Hubig, S. *J. Photochem.* **1985**, *30*, 121.
(6) Siampiringue, N.; Guyot, G.; Monti, S.; Bortolus, P. *J. Photochem.* **1987**, *37*, 185.
(7) Rau, H.; Lüddecke, E. *J. Am. Chem. Soc.* **1982**, *104*, 1616.
(8) Rau, H. *J. Photochem.* **1984**, *26*, 221.
(9) Rau, H.; Yu-Quan, S. *J. Photochem. Photobiol., A* **1988**, *42*, 321.
(10) Rau, H. In *Photochromism. Molecules and Systems*; Durr, H., Bouas-Laurent, H., Eds.; Elsevier: Amsterdam, 1990; Chapter 4, p 165.
(11) Horspool, W. In *The Chemistry of the Hydrazo, Azo and Azoxy Groups*; Patai, S., Ed.; Wiley: New York, 2000; Vol. 2.
(12) Lednev, I. K.; Ye, T.-Q.; Hester, R. E.; Moore, J. N. *J. Phys. Chem.* **1996**, *100*, 13338.
(13) Nägele, T.; Hoche, R.; Zinth, W.; Wachtveitl, J. *Chem. Phys. Lett.* **1997**, *272*, 489.
(14) Hamm, P.; Ohline, S. M.; Zinth, W. *J. Chem. Phys.* **1997**, *106*, 519.
(15) Lednev, I. K.; Ye, T.-Q.; Matousek, P.; Towrie, M.; Foggi, P.; Neuwahl, F. V. R.; Umapathy, S.; Hester, R. E.; Moore, J. N. *Chem. Phys. Lett.* **1998**, *290*, 68.
(16) Terazima, M.; Takezaki, M.; Yamaguchi, S.; Hirota, N. *J. Chem. Phys.* **1998**, *109*, 603.
(17) Tamai, N.; Miyasaka, H. *Chem. Rev.* **2000**, *100*, 1875.
(18) Fujino, T.; Tahara, T. *J. Phys. Chem. A* **2000**, *104*, 4203.
(19) Fujino, T.; Arzhantsev, S. Yu.; Tahara, T. *J. Phys. Chem. A* **2001**, *105*, 8123.
(20) Fujino, T.; Arzhantsev, S. Yu.; Tahara, T. *Bull. Chem. Soc. Jpn.* **2002**, *75*, 1031.
(21) Lu, Y.-C.; Chang, C.-W.; Diau, E. W.-G. *J. Chin. Chem. Soc.* **2002**, *49*, 693.
(22) Schultz, T.; Quenneville, J.; Levine, B.; Toniolo, A.; Martínez, T. J.; Lochbrunner, S.; Schmitt, M.; Schaffer, J. P.; Zgierski, M. Z.; Stolow, A. *J. Am. Chem. Soc.* **2003**, *125*, 8098.
(23) Satzger, H.; Spörlein, S.; Root, C.; Wachtveitl, J.; Zinth, W.; Gilch, P. *Chem. Phys. Lett.* **2003**, *372*, 216.
(24) Satzger, H.; Root, C.; Braun, M. *J. Phys. Chem. A* **2004**, *108*, 6265.
(25) Chang, C.-W.; Lu, Y.-C.; Wang, T.-T.; Diau, E. W.-G. *J. Am. Chem. Soc.* **2004**, *126*, 10109.
(26) Lu, Y.-C.; Diau, E. W.-G.; Rau, H. *J. Phys. Chem. A* **2005**, *109*, 2090.
(27) Stuart, C. M.; Frontiera, R. R.; Mathies, R. A. *J. Phys. Chem. A* **2007**, *111*, 12072.
(28) Monti, S.; Orlandi, G.; Palmieri, P. *Chem. Phys.* **1982**, *71*, 87.
(29) Cattaneo, P.; Persico, M. *Phys. Chem. Chem. Phys.* **1999**, *1*, 4739.
(30) Ishikawa, T.; Noro, T.; Shoda, T. *J. Chem. Phys.* **2001**, *115*, 7503.
(31) Diau, E. W.-G. *J. Phys. Chem. A* **2004**, *108*, 950.
(32) Gagliardi, L.; Orlandi, G.; Bernardi, F.; Cembran, A.; Garavelli, M. *Theor. Chem. Acc.* **2004**, *111*, 363.
(33) Cembran, A.; Bernardi, F.; Garavelli, M.; Gagliardi, L.; Orlandi, G. *J. Am. Chem. Soc.* **2004**, *126*, 3234.
(34) Ciminelli, C.; Granucci, G.; Persico, M. *Chem.—Eur. J.* **2004**, *10*, 2327.
(35) Barada, D.; Itoh, M.; Yatagai, T. *J. Appl. Phys.* **2004**, *96*, 4204.
(36) Toniolo, A.; Ciminelli, C.; Persico, M.; Martínez, T. J. *J. Chem. Phys.* **2005**, *123*, 234308.
(37) Crecca, C. R.; Roitberg, A. E. *J. Phys. Chem. A* **2006**, *110*, 8188.
(38) Granucci, G.; Persico, M. *Theor. Chem. Acc.* **2007**, *117*, 1131.
(39) Sauer, P.; Allen, R. E. *J. Phys. Chem. A* **2008**, *112*, 11142.
(40) Yuan, S.; Dou, Y.; Wu, W.; Hu, Y.; Zhao, J. *J. Phys. Chem. A* **2008**, *112*, 13326.
(41) Cusati, T.; Granucci, G.; Persico, M.; Spighi, G. *J. Chem. Phys.* **2008**, *128*, 194312.
(42) Creatini, L.; Cusati, T.; Granucci, G.; Persico, M. *Chem. Phys.* **2008**, *347*, 492.
(43) Ciminelli, C.; Granucci, G.; Persico, M. *Chem. Phys.* **2008**, *349*, 325.
(44) Conti, I.; Garavelli, M.; Orlandi, G. *J. Am. Chem. Soc.* **2008**, *130*, 5216.
(45) Wang, L.; Wu, W.; Yi, C.; Wang, X. *J. Mol. Graphics Modell.* **2009**, *27*, 792.
(46) Ootani, Y.; Satoh, K.; Nakayama, A.; Noro, T.; Taketsugu, T. *J. Chem. Phys.* **2009**, *131*, 194306.
(47) Tiberio, G.; Muccioli, L.; Berardi, R.; Zannoni, C. *ChemPhysChem* **2010**, *11*, 1018.
(48) Asakawa, M.; Ashton, P. R.; Balzani, V.; Brown, C. L.; Credi, A.; Matthews, O. A.; Newton, S. P.; Raymo, F. M.; Shipway, A. N.; Spencer, N.; Quick, A.; Stoddart, J. F.; White, A. J. P.; Williams, D. J. *Chem.—Eur. J.* **1999**, *5*, 860.
(49) Shipway, A. N.; Willner, I. *Acc. Chem. Res.* **2001**, *34*, 421.
(50) Ballardini, R.; Balzani, V.; Credi, A.; Gandolfi, M. T.; Venturi, M. *Acc. Chem. Res.* **2001**, *34*, 445.
(51) Dugave, C.; Demange, L. *Chem. Rev.* **2003**, *103*, 2475.
(52) Cojocariu, C.; Rochon, P. *Pure Appl. Chem.* **2004**, *76*, 1479.
(53) Yager, K. G.; Barrett, C. J. *J. Photochem. Photobiol., A* **2006**, *182*, 250.
(54) Browne, W. R.; Feringa, B. L. *Nat. Nanotechnol.* **2006**, *1*, 25.
(55) Camorani, P.; Fontana, M. P. *Phys. Rev. E* **2006**, *73*, 011703.
(56) Vecchi, I.; Arcioni, A.; Bacchiocchi, C.; Tiberio, G.; Zanirato, P.; Zannoni, C. *J. Phys. Chem. B* **2007**, *111*, 3355.
(57) Ambrosio, A.; Camposino, A.; Maddalena, P.; Patané, S.; Allegrini, M. *J. Microsc.* **2008**, *229*, 307.
(58) Rais, D.; Zakrevskyy, Y.; Stumpe, J.; Nešpøurek, S.; Sedláková, Z. *Opt. Mater.* **2008**, *30*, 1335.
(59) Ferri, V.; Elbing, M.; Pace, G.; Dickey, M. D.; Zharnikov, M.; Samor, P.; Rampi, M. A. *Angew. Chem., Int. Ed.* **2008**, *47*, 4307.
(60) Sasaki, T.; Tour, J. M. *Org. Lett.* **2008**, *10*, 897.
(61) Yamada, M.; Kondo, M.; Mamiya, J.; Yu, Y.; Kinoshita, M.; Barrett, C. J.; Ikeda, T. *Angew. Chem., Int. Ed.* **2008**, *47*, 4986.
(62) Oki, K.; Nagasaka, Y. *Colloids Surf., A* **2009**, *333*, 182.
(63) Savoini, M.; Biagioni, P.; Duò, L.; Finazzi, M. *Opt. Lett.* **2009**, *34*, 761.
(64) Domenici, V.; Ambrožic, G.; Čopic, M.; Lebar, A.; Drevenšek-Olenik, I.; Umek, P.; Zalar, B.; Zupančič, B.; Žigon, M. *Polymer* **2009**, *50*, 4837.
(65) Devetak, M.; Zupančič, B.; Lebar, A.; Umek, P.; Zalar, B.; Domenici, V.; Ambrožic, G.; Žigon, M.; Čopic, M.; Drevenšek-Olenik, I. *Phys. Rev. E* **2009**, *80*, 050701.
(66) Yoshino, T.; Kondo, M.; Mamiya, J.; Kinoshita, M.; Yu, Y.; Ikeda, T. *Adv. Mater.* **2010**, *22*, 1361.
(67) Basheer, M. C.; Oka, Y.; Mathews, M.; Tamaoki, N. *Chem.—Eur. J.* **2010**, *16*, 3489.
(68) Ji, M.; Li, Y.; White, T.; Urbas, A.; Li, Q. *Chem. Commun.* **2010**, *46*, 3463.
(69) Tully, J. C. *J. Chem. Phys.* **1990**, *93*, 1061.
(70) Granucci, G.; Persico, M.; Toniolo, A. *J. Chem. Phys.* **2001**, *114*, 10608.
(71) Ben-Nun, M.; Martínez, T. J. *Adv. Chem. Phys.* **2002**, *121*, 439.
(72) Granucci, G.; Persico, M. *J. Chem. Phys.* **2007**, *126*, 134114.
(73) Stewart, J. J. P. *MOPAC*; Fujitsu Limited: Tokyo, Japan, 2002.
(74) Cusati, T.; Granucci, G.; Martínez-Núñez, E.; Martini, F.; Persico, M.; Vázquez, S. Manuscript in preparation.
(75) Andersson, J.-Å.; Petterson, R.; Tegnér, L. *J. Photochem.* **1982**, *20*, 17.
(76) Adamson, A. W.; Wachter, R. *J. Am. Chem. Soc.* **1978**, *100*, 1298.
(77) Jorgensen, W. L.; Tirado-Rives, J. *J. Am. Chem. Soc.* **1988**, *110*, 1657.
(78) Kony, D.; Damm, W.; Stoll, S.; Van Gunsteren, W. F. *J. Comput. Chem.* **2002**, *23*, 1416.
(79) de Oliveira, O. V.; Gomide Freitas, L. C. *J. Mol. Struct. THEOCHEM* **2005**, *728*, 179.

(80) Persico, M.; Granucci, G.; Inglese, S.; Laino, T.; Toniolo, A. *J. Mol. Struct. THEOCHEM* **2003**, *621*, 119.
(81) Ponder, J. W. *TINKER 4.1*; Washington University School of Medicine: St. Louis, MO: 2004. http://dasher.wustl.edu/tinker.
(82) Cattaneo, P.; Granucci, G.; Persico, M. *J. Phys. Chem. A* **1999**, *103*, 3364.
(83) Paschek, D.; Geiger, A. *MOSCITO 3.9*; Department of Physical Chemistry, University of Dortmund: 2000.
(84) Thomas, L. L.; Christakis, T. J.; Jorgensen, W. L. *J. Phys. Chem. B* **2006**, *110*, 21198.
(85) Yamaguchi, T.; Hidaka, K.; Soper, A. K. *Mol. Phys.* **1999**, *97*, 603.
(86) Lide, D. R. *CRC Handbook of Chemistry and Physics*; 78th ed.; CRC: Boca Raton, 1997.
(87) Malhado, J. P.; Spezia, R.; Hynes, J. T. *J. Phys. Chem. A* **2011**10.1021/jp106096m.
(88) Böckmann, M.; Doltsinis, N. L.; Marx, D. *Phys. Rev. E* **2008**, *78*, 036101.
(89) Böckmann, M.; Doltsinis, N. L.; Marx, D. *J. Phys. Chem. A* **2010**, *114*, 745.